

Deteriorated Interlayer Coupling in Twisted Bilayer Cobaltites

*Dongke Rong,^{†,‡,◇} Xiuqi Chen,^{†,‡,◇} Shengru Chen,^{†,‡,△,◇} Jingfeng Zhang,[§] Yue Xu,^{†,‡},
Yanxing Shang,^{†,‡} Haitao Hong,^{†,‡} Ting Cui,^{†,‡} Qianying Wang,^{†,‡} Chen Ge,^{†,‡} Can Wang,
^{†,‡} Qiang Zheng,^{||} Qinghua Zhang,^{†,‡} Lingfei Wang,[§] Yu Deng,^{⊥,*} Kuijuan Jin,^{†,‡,*} Gang-
Qin Liu,^{†,‡,*} and Er-Jia Guo^{†,‡,*}*

Affiliations:

[†] Beijing National Laboratory for Condensed Matter Physics and Institute of Physics,
Chinese Academy of Sciences, Beijing 100190, China

[‡] Department of Physics & Center of Materials Science and Optoelectronics Engineering,
University of Chinese Academy of Sciences, Beijing 100049, China

[△] School of Physics, Zhejiang University, Hangzhou, China

[§] Hefei National Research Center for Physical Sciences at Microscale, University of Science
and Technology of China, Hefei 230026, China

^{||} CAS Key Laboratory of Standardization and Measurement for Nanotechnology, CAS
Center for Excellence in Nanoscience, National Centre for Nanoscience and Technology,
Beijing 100190, China

[⊥] National Laboratory of Solid-state Microstructures, Jiangsu Key Laboratory of Artificial
Functional Materials, College of Engineering and Applied Sciences, Collaborative Innovation
Center of Advanced Microstructures, Nanjing, Jiangsu 210023, China

KEYWORDS: twistrionics, magnetic coupling, freestanding membranes, moiré pattern

ABSTRACT

A wealth of remarkable behaviors is observed at the interfaces between magnetic oxides due to the coexistence of Coulomb repulsion and interatomic exchange interactions. While previous research has focused on bonded oxide heterointerfaces, studies on magnetism in van der Waals interfaces remain rare. In this study, we stacked two freestanding cobaltites with precisely controlled twist angles. Scanning transmission electron microscopy revealed clear and ordered moiré patterns, which exhibit an inverse relationship with the twist angle. We found that the Curie temperature in the twisted region is reduced by approximately 13 K compared to the single-layer region using nitrogen-vacancy (NV) magnetometry. This phenomenon may be related to the weakening of the orbital hybridization between oxygen ions and transition metal ions in the unbonded interfaces. Our findings suggest a potential avenue for modulating magnetic interactions in correlated systems through twist, providing opportunities for the discovery of unknown quantum states.

MAIN TEXT

Magnetic coupling at interfaces plays a pivotal role in the functionality of spintronic devices. For example, interlayer RKKY interactions and exchange bias effects are essential for stabilizing the magnetic reference layer in magnetic tunnel junctions (MTJs).¹⁻⁵ Meanwhile, interlayer magnetic dipole coupling and chiral interactions hold promise for the development of novel computing devices, such as magnetic logic circuits and neuromorphic computing units.⁶⁻⁹ Current research on interlayer magnetic coupling predominantly focuses on chemically bonded heterointerfaces between magnetic or non-magnetic materials, including complex metal oxide heterostructures.¹⁰⁻¹⁶ These interfaces, formed through covalent or ionic bonds, exhibit a diverse array of novel magnetic phenomena distinct from those of the parent materials. Observed interfacial phenomena, such as charge transfer, spin-orbit coupling, and lattice structure regulation, arise from the intricate interactions between transition metal ions mediated by anions.

Beyond conventional bonded magnetic interfaces, van der Waals (vdW) magnetic interfaces and their associated physical properties remain largely unexplored. The atomic distance between the magnetic layers in these systems is larger than that within the layers, leading to complex magnetic interactions that depend on factors such as the number of atomic layers and the stacking order of the material.^{17, 18} Although numerous studies have demonstrated intriguing magnetic coupling in two-dimensional (2D) magnetic materials like Cr₂Ge₂Te₆, CrI₃, and CrSBr, among others,¹⁹⁻²⁶ vdW magnetic interfaces in complex oxides have been scarcely investigated. Recent advances have introduced new methods for fabricating freestanding oxide membranes.^{27, 28} These membranes, akin to 2D materials, offer extreme

flexibility and can be tailored by controlling stacking sequences and twist angles between subsequent layers. Unlike traditional oxide heterostructures, stacking freestanding oxide membranes does not require lattice matching or the formation of chemical bonds, allowing layers with different lattice symmetries and atomic spacings to be combined. The vdW interfaces formed between these freestanding oxide membranes are expected to differ significantly from conventional oxide heterointerfaces. Twisting these membranes can generate moiré patterns, similar to those seen in twisted 2D materials, opening up new avenues for exploring unique atomic structures and physical properties.²⁹⁻³¹ While previous studies have focused on the atomic arrangements in twisted oxide membranes with controllable twist angles,^{32,33} the exploration of artificially twisted stacking in vdW magnetic oxide membranes, particularly those with complex ion-covalent bonds, remains unexplored. This presents an intriguing research frontier and an important direction for future investigation.

In this study, we fabricated high-quality, single-crystalline $\text{La}_{0.8}\text{Sr}_{0.2}\text{CoO}_3$ (LSCO) freestanding membranes using a water-soluble sacrificial layer. Distinct and periodic moiré patterns were observed in the twisted LSCO bilayer membranes, with the spacing and size of the moiré patterns being inversely proportional to the twist angle between the crystallographic axes of the constituent layers. Nanoscale magnetic probing revealed a reduced magnetic transition temperature in the twisted region, indicating that twistronics offers a new degree of freedom for designing and engineering oxide interface phenomena.

Results and discussions

The water-soluble sacrificial layer $\text{Sr}_4\text{Al}_2\text{O}_7$ (T-SAO)²⁸ and the magnetic LSCO layer were epitaxially grown on (001)-oriented $(\text{LaAlO}_3)_{0.3}\text{-(Sr}_2\text{AlTaO}_6)_{0.7}$ (LSAT) substrates using pulsed

laser deposition (PLD) (see Methods). The structural properties of LSCO were characterized using an x-ray diffractometer (XRD) before release from the substrates. Both LSCO and T-SAO films exhibited distinct Laue oscillations, indicating extremely high crystallinity and successful epitaxial growth (Figure S1). The out-of-plane lattice constant (c) of as-grown LSCO is approximately 3.805 Å, suggesting the LSCO films suffer an in-plane tensile strain. Following the conventional transfer method, we were able to attach an LSCO freestanding membrane onto a bare Al₂O₃ substrate. An XRD 2 θ - ω scan revealed a single-crystalline LSCO membrane, which exhibited an increased c to 3.835 Å due to the release of epitaxial tensile strain. Thus, the freestanding LSCM membranes are free of substrate's clamping induced epitaxial strain effects.

To obtain a substantial portion of LSCO freestanding membranes, we employed an alternative transfer technique that can be readily applied to various supports, as illustrated in Figure S2 and detailed see Methods. The structural properties of twisted BL LSCO were investigated by planar-view high-angle annular dark field (HAADF) scanning transmission electron microscopy (STEM) experiments (Figure 1a). We intentionally selected the sample edge area to include single layer (SL), BL, and multi-layer regions within a single region (Figure S3). For non-twisted BL LSCO, where the twist angle α is approximately 0°, the upper and lower LSCO lattices overlap in a highly coincidental (atom-on-atom) manner. We present a detailed simulation analysis of twisted oxide bilayers (Figure S4). The simulation results clearly demonstrate that the HAADF image and Moiré pattern can identify structural modifications in bilayers with a twist angle as small as 0.1°. Therefore, if the twist angle is not precisely 0°, it is likely below 0.1°, which is indistinguishable and therefore negligible in its

influence. The color difference due to mass-thickness contrast was visible during STEM imaging, with darker regions corresponding to the SL LSCO membrane and brighter regions to the non-twisted BL LSCO membrane. These regions were separated by an atomically sharp boundary. The atomic arrangement of LSCO unit cells is depicted in Figure 1b, where La/Sr atoms occupy the A-site, Co atoms are located at the B-site, and O atoms form the octahedra. Figure 1c presents the line profiles of HAADF intensity across the SL and BL LSCO regions. The thickness of the upper LSCO membranes is approximately 5 nm, which is consistent with the thickness determined by PLD growth. The gap distance between twisted BL LSCO, depending on the transfer process, does not keep constant. We average the distance is approximately 2 ± 0.5 nm (Figure S5). We understand that the gap maybe a bit wide for a dipole-dipole interaction. Please note that the roughness and step-and-terrace of LSCO membranes is approximately 1-2 unit-cells. Thus, the magnetic coupling between twisted LSCO still valid.

For twisted BL LSCO, the characteristic moiré features were observed. Figure 1e presents a representative STEM image that includes both SL and twisted BL regions. Although the α was pre-set during the transfer process, the exact twist angle of the stacked freestanding membranes was determined in two independent methods. The first method involves measuring the twist angle between the two scattering vectors directly from the fast Fourier transform (FFT) image. The second method involves measuring the real space distance ($d_{\text{moiré}}$) of the moiré fringes and d_{vector} . The twist angle is then calculated using the formular $\alpha = 2 \sin^{-1} d_{\text{vector}}/2d_{\text{moiré}}$. In Figure 1e, $d_{\text{vector}} = 1.925$ Å for the (200) scattering vector and $d_{\text{moiré}} = 14.91$ Å, resulting in $\alpha \sim 7.4^\circ$. The calculated twist angle is consistent with both the FFT

result and the pre-set misalignment angle. We further investigated the structural properties of moiré patterns formed at a twist angle of $\alpha = 4^\circ, 7.4^\circ, 9^\circ, 12^\circ, 19^\circ,$ and 39° twisted BL LSCO membranes. The STEM-HAADF images and their corresponding FFT results are summarized in Figures 2a and 2b, respectively. Periodic moiré patterns, marked by dashed yellow squares, are observed in all twisted BL LSCO membranes. The spacing and size of the moiré patterns progressively decrease with increasing twist angles. In the FFT images, two sets of diffraction spots, indicated by red and blue rectangles, confirm the overlapping of two LSCO freestanding membranes with a misorientation. We also simulated the moiré patterns and corresponding FFT results with different twist angles (Figure S6). Both experiments and simulations are consistent with each other. Similarly, we employed two calculation methods to determine and verify the twist angles of each BL LSCO. Specifically, Figure 2c presents a zoomed-in view of a representative single moiré pattern from a twisted BL LSCO with $\alpha = 19^\circ$. The bright white spots correspond to La/Sr atoms, while the Co atoms are less distinct, and the O atoms are invisible due to the HAADF intensity scaling with the atomic number of the elements.

To elucidate the atomic arrangement in the twisted BL LSCO, a 3×3 unit-cell model with $\alpha = 19^\circ$ was constructed for direct comparison with our measured HAADF image (Figure 2d). The dependence of the moiré pattern area (A^2) and spacing (λ) on the twist angle is summarized in Figures 2e and 2f, respectively. Typically, the moiré effect occurs when two periodic layers are superimposed and the general relationship is $\lambda \sim \frac{(1+\delta)\alpha}{\sqrt{2(1+\delta)(1-\cos \alpha)+\delta^2}}$, where δ is the lattice mismatch between the two layers.^{34, 35} When two layers are made of same material with identical lattice parameters, the formula can be simplified to $\lambda \sim \frac{a}{2\sin(\frac{\alpha}{2})}$. We find that both parameters in our twist BL LSCO follow the reciprocal relation to $\frac{a}{2\sin(\frac{\alpha}{2})}$ and $\left(\frac{a}{2\sin(\frac{\alpha}{2})}\right)^2$ for λ

and A^2 , respectively. The $\lambda \sim \frac{a}{2\sin(\frac{\alpha}{2})}$ relationship agrees well with previously reported twist 2D materials, such as twist bilayer graphene (tBLG), twist graphene-hBN heterostructure and others transition metal dichalcogenides (TMDs).^{19, 36-38} Early work demonstrated that a special critical twist angles can generate novel physics, such as flat band, superconductivity, and correlated insulating state, due to the strong correlated electron interaction. Although the crystal structure and symmetry of perovskite LSCO is different from the hexagonal lattice of graphene and TMDs, they all follow the same rule: $\lambda \sim \frac{a}{2\sin(\frac{\alpha}{2})}$, confirming the universal moiré effect from a geometric point of view.

In addition to the moiré patterns observed in the twisted BL LSCO, it is noteworthy that moiré stripes are formed within the BL LSCO (Figure S7). These stripes have a width of approximately 2 nm and align at 45° with respect to both the (100) and (010) orientations of the SL LSCO. We ruled out the possibility of a tilted zone axis during the STEM imaging process. We meticulously simulated the tilt patterns of BL LSCO with various tilted zone axes (Figure S8). To generate a stripe with a width as narrow as 2 nm, the zone axis would need to be increased to at least 400 mrad, which clearly does not apply to our case. Thus, we attribute the observed phenomena to the lateral shift of the upper LSCO layer. The clear structural variation with the twist angle opens up new avenues for engineering correlated electron systems using "*moiré modulation*" as an important degree of freedom.

Our previous work demonstrated that freestanding membranes, when attached to one another, form a space layer with a thickness of at least 1 nm, even after being heated to the growth temperature (typically 800 °C).^{39, 40} This result suggests that no chemical bonds are formed between the two LSCO membranes; instead, vdW interactions may still occur at the

interfaces. A recent study by Sánchez-Santolino *et al.*³³ reported that lateral strain modulation forms between twisted freestanding ferroelectric oxides due to interface matching. They found that the nanoscale-modulated distribution of shear strain drives notable polar vortices and antivortex structures, which appear to change with the twist angle. To our knowledge, this report is the first experimental evidence that vdW interactions between twisted membranes can lead to moiré-related phenomena. To study the magnetic interactions at vdW interfaces formed in twisted BL LSCO, we performed spatially resolved magnetic measurements using a home-built optically detected magnetic resonance (ODMR) system. As shown in Figure 3a, a layer of shallow nitrogen-vacancies (NV centers) in a high-purity diamond (Element Six, with an initial nitrogen concentration of 5 ppb) serves as *in-situ* quantum sensors. The NV centers were generated by nitrogen ion implantation with an energy of 10 keV and a dose of 5×10^{13} ions/cm² and subsequent high-temperature annealing (1000 °C for 70 mins). The density of these NV centers was estimated to be approximate 60 ppb, with a spin coherence time $T_2 = 1.31(6) \mu\text{s}$. The twisted BL LSCO with $\alpha = 8^\circ$ were transferred to the diamond substrate before the measurements. After loading the sample, the regions of interest were addressed with both the brightfield optical image and the confocal laser scanning image.

Figure 3b shows the comparison of ODMR spectra from both SL and BL LSCO regions at different temperatures (more results are shown in Figure S9). At low temperatures, the ODMR spectra split with a magnitude of $2\gamma B$, where $\gamma = 2.802 \text{ MHz/Gauss}$ is the gyromagnetic ratio of NV electron spin and B is the magnetic stray field from the LSCO film. Figures 3e and 3f summarize the temperature-dependent ODMR splitting for SL and BL LSCO membranes, respectively. The ODMR splitting for BL LSCO increases nearly twice as much as that of SL

LSCO, indicating that the net magnetic moment increases when the layer thickness doubled. We fit the $2\gamma B-T$ curve with the Curie-Weiss law. Interestingly, we found that the magnetic transition temperatures (T_C) are approximately 187 K and 200 K for BL and SL LSCO, respectively. These results were repeated at different positions in both SL and BL LSCO (Figure S10), suggesting the robust reduction of T_C after stacking two BL with a twist angle. Since the ensemble NV centers are measured in single laser spots, the gradient of the stray field also leads to a significant broadening of the ODMR spectra. Here, the ODMR width also shows a clear temperature dependence with a lower T_C for the BL region (Figure S11). The T_C of LSCO films is known to increase with film thickness.^{41,42} Finite-size scaling is particularly evident in films with thicknesses below 40 nm. However, our findings indicate that the T_C for BL LSCO is reduced compared to SL LSCO, which contrasts with the expected effects of doubling the film thickness. We attribute this observed reduction in T_C to the magnetic coupling between the LSCO layers.

Since the major impact factors, such as epitaxial strain, Sr concentration, and film thickness,⁴³⁻⁴⁵ are constant for BL and SL LSCO, leaving twist angle is a single parameter that affects the magnetic properties of BL LSCO. Previously, Xie *et al.* report a reduction of ~ 20 K of the Néel temperature is observed in the 1.1° twist 2D magnetic CrI_3 , compared with natural CrI_3 .⁴⁶ They attribute this to the moiré superlattice-induced magnetic competition. The emergence of non-collinear spins in the twisted CrI_3 modulates the interlayer coupling, leading to the reduction of critical temperature. Our result shows similar reduced T_C in twisted BL LSCO, suggesting the weakening of magnetic intercoupling between two freestanding membranes. However, unfortunately, the exact spin structure and magnetic interaction in the

twisted BL LSCO is much more complex than in 2D materials due to the correlated electron system. Previous research has shown that the ordering of Co-3*d* orbitals is responsible for the ferromagnetism observed in cobaltites. Consequently, one potential scenario is that the hypothesized reconstruction of orbital ordering, achieved by twisting two LSCO layers, could influence the magnetic exchange interactions, potentially leading to a reduction in the magnetic ordering temperature. Similar behaviors have been observed in other perovskite oxides, where the transition temperature of the orbital order increases while the magnetic order decreases.^{47,48} Another possibility is the influence of phase separation at the twisted LSCO interfaces. This instability is promoted by a reduction in carriers, which weakens the ferromagnetic coupling between Co ions and enhances the relevance of superexchange antiferromagnetic interactions. Although further experimental and theoretical investigations are necessary to fully understand the microscopic nature of these complex electronic order phases at the interfaces, the current findings offer valuable insights into the critical surface/interface sensitivity of orbitally-active twisted LSCO.

For the twisted BL LSCO, we still need to understand exactly how the magnetic exchange interaction varies with the twist angle. It is certainly both interesting and important to map the evolution of magnetic properties—such as saturation moment, critical temperature, and anisotropy—as a function of twist angle. This is not merely a simple method for tuning physical properties; more importantly, it is crucial to understand how the coupling strength of interfacial magnetic exchange interaction changes under different stacking orders at the interface. Unfortunately, conducting NV magnetometry measurements at cryogenic temperatures for all twist angles requires a significant amount of time and effort (several months for our setups)

because we need to prepare diamond substrates with significant NV centers and transfer BL LSCO successfully on them. Recent years, the scanning NV microscopy at cryogenic temperatures has also facilitated the study of magnetic domain structures and magnetic fluctuation around the Curie temperatures, especially in two-dimensional ferromagnetic or antiferromagnetic materials. It is not only a highly sensitive magnetic detection method but also possesses ultra-high spatial resolution, which can help us to investigate the evolution of magnetic domains in twisted and non-twisted regions under external fields, including coercivity, domain wall motions, magnetic reversal time, and so on. Furthermore, the development of new theoretical methods and computational tools is essential for understanding vdW correlated magnetic interfaces, which is also one of the key development directions in future.

Furthermore, we noted that the potential ferroelectric characteristics were observed in the twisted oxide systems³³. We conducted an analysis of the strain modulation in a representative twisted bilayer LSCO, as illustrated in Figure S12. The shear strain mapping reveals a periodic strain modulation within the top LSCO layer. The intralayer strain of the top layer was measured using the entrance surface-focused image method.³³ This strain modulation is closely associated with intralayer matching, displaying the same periodicity as the Moiré pattern. Therefore, we demonstrated that both ferroelectric and ferromagnetic orders coexist in BL LSCO, which would constitute a novel single-phase multiferroic system. Thus, this experimental result suggests that twisted systems offer a new perspective for the study of novel multiferroic materials.

In summary, we successfully fabricated twisted bilayer LSCO membranes with controllable twist angles. High-resolution scanning transmission electron microscopy revealed

clear and ordered moiré patterns. The period and area of the moiré patterns exhibit a reciprocal relationship with the twist angle, which is consistent with the universal rule $\lambda \sim \frac{a}{2\sin(\frac{\alpha}{2})}$ in twisted moiré structures. NV magnetometry measurements indicate a reduction in the Curie temperature by approximately 10 K in twisted BL LSCO compared to single-layer LSCO, suggesting weakened magnetic coupling at the van der Waals interface between the LSCO membranes. Our results suggest that the twist angle can serve as a novel degree of freedom for modulating magnetic interactions in correlated systems.

FIGURES AND FIGURE CAPTIONS

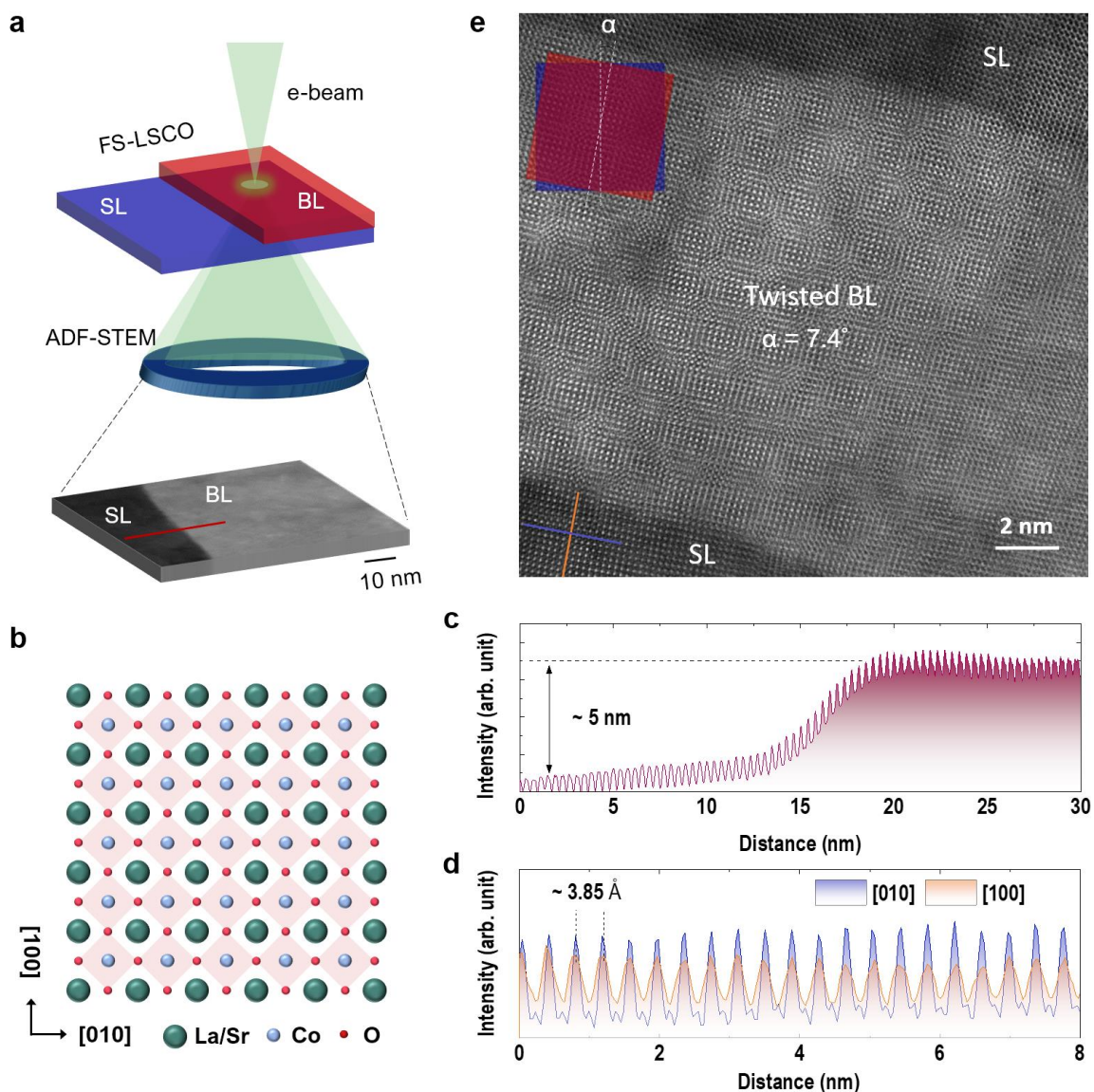


Figure 1. Structural characterization of twisted BL LSCO. (a) Schematic of atomic structure imaging via HAADF-STEM. (b) Schematic of a perovskite-type LSCO, exhibiting isotropy along (100) and (010) orientations. (c) Intensity profile obtained from line scans averaged across SL and BL regions in (a), indicating an intensity increase in the BL region due to a thickness increase of approximately 5 nm. (d) Averaged intensity profile lines extracted from (010) and (100) orientations at the SL region, revealing a lattice constant of 3.85 Å in both orientations, confirming the in-plane isotropy of the SL LSCO membranes. (e) High-resolution STEM image depicting the LSCO membranes with a single layer (SL) region and a twisted bilayer (BL) region at a rotation angle $\alpha = 7.4^\circ$. The white scale bar denotes 2 nm.

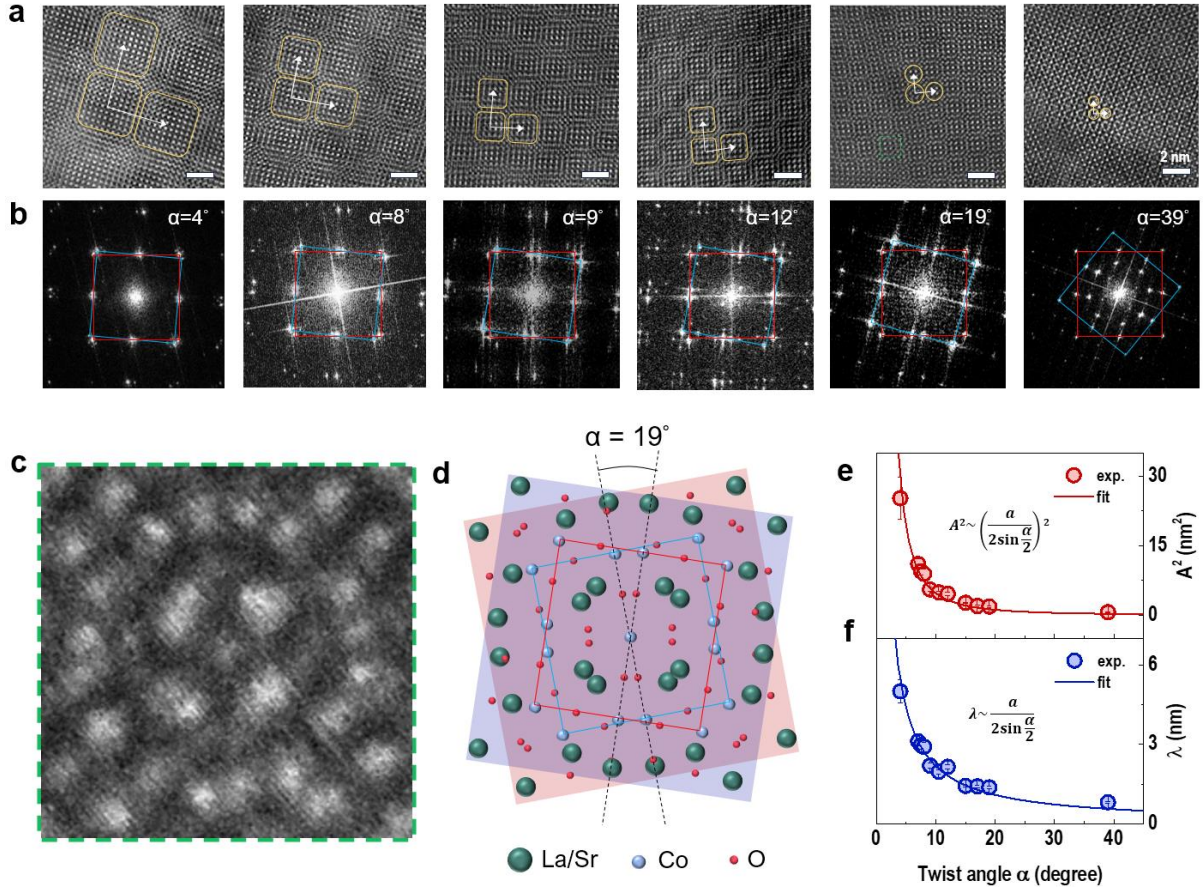


Figure 2. Evolution of moiré patterns in twisted BL LSCO. (a) High-resolution STEM images and (b) corresponding fast Fourier transform (FFT) images from BL LSCO membranes with various twist angles (α). Moiré patterns and their closest neighbors are indicated by yellow boxes in (a). Two distinct sets of diffraction spots, highlighted by red and blue squares, elucidate the twisted structure from BL LSCO. (c) A zoom-in STEM image from a moiré pattern with $\alpha = 19^\circ$. The atomic arrangement is illustrated in (d). (e) and (f) show the area (A^2) of moiré patterns and the average distance (λ) between adjacent moiré patterns as a function of α , respectively.

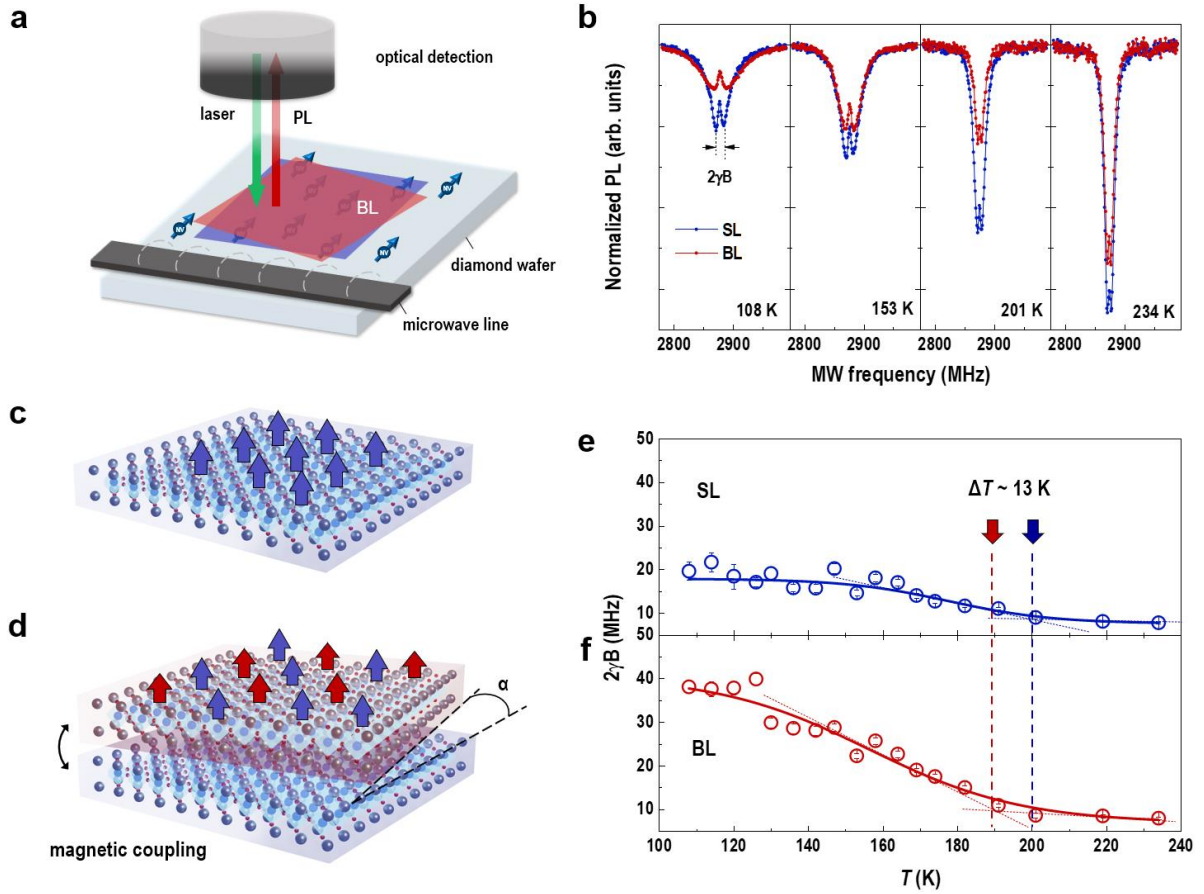


Figure 3. Spatially resolved magnetization of twisted BL LSCO. (a) Schematic of NV magnetometry. (b) Comparison of ODMR spectra recorded at SL and BL regions at different temperatures. All peaks split with a magnitude of $2\gamma B$, where $\gamma=2.802$ MHz/Gauss is the gyromagnetic ratio of the NV electron spin and B is the local magnetic field. (c) and (d) Schematic illustrations of magnetic interactions at SL and BL regions with $\alpha = 8^\circ$, respectively. (e) and (f) Temperature-dependent ODMR splitting at SL and BL regions, respectively. We find that the ferromagnetic-paramagnetic phase transition temperatures for SL and BL vary by approximate 10 K. Colored dashed lines are the linearly fits to the curves at FM and PM regimes.

ASSOCIATED CONTENT

Supporting Information

The Supporting Information is available free of charge via the internet at <http://pubs.acs.org>.

Details on the structural characterizations, STEM sample preparation process, zoom-out STEM images, diffraction pattern simulations, temperature-dependent ODMR spectra are supplied as supporting information.

AUTHOR INFORMATION

Corresponding authors

*Emails: kjjin@iphy.ac.cn, dengyu@nju.edu.cn, gqliu@iphy.ac.cn, and ejguo@iphy.ac.cn

Author contributions

◇ D. Rong, X. Chen, and S. Chen contributed equally to the manuscript. E.J.G initiated the research and supervised the project. These samples were grown by S.R.C., J.F.Z., D.K.R., H.T.H., T.C., Q.Y.W. under supervision of E.J.G. and L.F.W.; TEM lamellas were fabricated with FIB milling and TEM experiments were performed by Q.Z., Q.H.Z., and Y.D.; NV magnetometry measurements were performed by X.C., Y.X., Y.S. under supervision of G.Q.L.; D.K. and E.J.G. wrote the manuscript. All authors participated in the discussion of manuscript.

Notes

The authors declare no competing financial interest.

ACKNOWLEDGEMENTS

We thank the fruitful discussions with Prof. Guoqiang Yu, Prof. Yang Xu, and Prof. Wei Yang (IOP-CAS), Prof. Yu Ye (Peking University), Prof. Jinxing Zhang (Beijing Normal University), and Prof. Houbin Huang (Beijing Institute of Technology). This work was supported by the

National Key Basic Research Program of China (Grant Nos. 2020YFA0309100 and 2019YFA0308500), the National Natural Science Foundation of China (Grant Nos. U22A20263, 52250308, and 12304158), the Beijing Natural Science Foundation (Grant No. JQ24002), the CAS Project for Young Scientists in Basic Research (Grant No. YSBR-084), the China Postdoctoral Science Foundation (Grant No. 2022M723353), the Chinese Academy of Sciences (CAS) Project for Young Scientists in Basic Research (Grant No. YSBR-084), the CAS Youth Interdisciplinary Team, the Special Research assistant and Strategic Priority Research Program (B) (Grant No. XDB33030200) of CAS.

REFERENCES

- (1) Zutic, I.; Fabian, J.; Das Sarma, S. Spintronics: Fundamentals and applications. *Rev. Mod. Phys.* **2004**, 76 (2), 323-410.
- (2) Wolf, S. A.; Awschalom, D. D.; Buhrman, R. A.; Daughton, J. M.; von Molnár, S.; Roukes, M. L.; Chtchelkanova, A. Y.; Treger, D. M. Spintronics:: A spin-based electronics vision for the future. *Science* **2001**, 294 (5546), 1488-1495.
- (3) Chappert, C.; Fert, A.; Van Dau, F. N. The emergence of spin electronics in data storage. *Nat. Mater.* **2007**, 6 (11), 813-823.
- (4) Park, B. G.; Wunderlich, J.; Martí, X.; Holy, V.; Kurosaki, Y.; Yamada, M.; Yamamoto, H.; Nishide, A.; Hayakawa, J.; Takahashi, H.; Shick, A. B.; Jungwirth, T. A spin-valve-like magnetoresistance of an antiferromagnet-based tunnel junction. *Nat. Mater.* **2011**, 10 (5), 347-351.
- (5) Parkin, S. S. P.; Roche, K. P.; Samant, M. G.; Rice, P. M.; Beyers, R. B.; Scheuerlein, R. E.; O'Sullivan, E. J.; Brown, S. L.; Bucchigano, J.; Abraham, D. W.; Lu, Y.; Rooks, M.; Trouilloud,

- P. L.; Wanner, R. A.; Gallagher, W. J. Exchange-biased magnetic tunnel junctions and application to nonvolatile magnetic random access memory (invited). *J. Appl. Phys.* **1999**, *85* (8), 5828-5833.
- (6) Chumak, A. V.; Vasyuchka, V. I.; Serga, A. A.; Hillebrands, B. Magnon spintronics. *Nat. Phys.* **2015**, *11* (6), 453-461.
- (7) Cavin, R. K.; Lugli, P.; Zhirnov, V. V. Science and Engineering Beyond Moore's Law. *Proc. IEEE* **2012**, *100*, 1720-1749.
- (8) Nayak, A. K.; Kumar, V.; Ma, T. P.; Werner, P.; Pippel, E.; Sahoo, R.; Damay, F.; Rössler, U. K.; Felser, C.; Parkin, S. S. P. Magnetic antiskyrmions above room temperature in tetragonal Heusler materials. *Nature* **2017**, *548* (7669), 561-+.
- (9) Grollier, J.; Querlioz, D.; Camsari, K. Y.; Everschor-Sitte, K.; Fukami, S.; Stiles, M. D. Neuromorphic spintronics. *Nat. Electron.* **2020**, *3* (7), 360-370.
- (10) Chen, S. R.; Zhang, Q. H.; Li, X. J.; Zhao, J. L.; Lin, S.; Jin, Q.; Hong, H. T.; Huon, A.; Charlton, T.; Li, Q.; Yan, W. S.; Wang, J. O.; Ge, C.; Wang, C.; Wang, B. T.; Fitzsimmons, M. R.; Guo, H. Z.; Gu, L.; Yin, W.; Jin, K. J.; Guo, E. J. Atomically engineered cobaltite layers for robust ferromagnetism. *Sci. Adv.* **2022**, *8* (43), 9.
- (11) Li, S. S.; Zhang, Q. H.; Lin, S.; Sang, X. H.; Need, R. F.; Roldan, M. A.; Cui, W. J.; Hu, Z. Y.; Jin, Q.; Chen, S.; Zhao, J. L.; Wang, J. O.; Wang, J. S.; He, M.; Ge, C.; Wang, C.; Lu, H. B.; Wu, Z. P.; Guo, H. Z.; Tong, X.; Zhu, T.; Kirby, B.; Gu, L.; Jin, K. J.; Guo, E. J. Strong Ferromagnetism Achieved via Breathing Lattices in Atomically Thin Cobaltites. *Adv. Mater.* **2021**, *33* (4), 9.
- (12) Liao, Z.; Huijben, M.; Zhong, Z.; Gauquelin, N.; Macke, S.; Green, R. J.; Van Aert, S.;

Verbeeck, J.; Van Tendeloo, G.; Held, K.; Sawatzky, G. A.; Koster, G.; Rijnders, G. Controlled lateral anisotropy in correlated manganite heterostructures by interface-engineered oxygen octahedral coupling. *Nat. Mater.* **2016**, 15 (4), 425-+.

(13) Kan, D.; Aso, R.; Sato, R.; Haruta, M.; Kurata, H.; Shimakawa, Y. Tuning magnetic anisotropy by interfacially engineering the oxygen coordination environment in a transition metal oxide. *Nat. Mater.* **2016**, 15 (4), 432-+.

(14) Borisov, P.; Hochstrat, A.; Chen, X.; Kleemann, W.; Binek, C. Magnetoelectric switching of exchange bias. *Phys. Rev. Lett.* **2005**, 94 (11), 4.

(15) Ohtomo, A.; Hwang, H. Y. A high-mobility electron gas at the LaAlO₃/SrTiO₃ heterointerface. *Nature* **2004**, 427 (6973), 423-426.

(16) Wang, J.; Neaton, J. B.; Zheng, H.; Nagarajan, V.; Ogale, S. B.; Liu, B.; Viehland, D.; Vaithyanathan, V.; Schlom, D. G.; Waghmare, U. V.; Spaldin, N. A.; Rabe, K. M.; Wuttig, M.; Ramesh, R. Epitaxial BiFeO₃ multiferroic thin film heterostructures. *Science* **2003**, 299 (5613), 1719-1722.

(17) Sun, Z. Y.; Yi, Y. F.; Song, T. C.; Clark, G.; Huang, B.; Shan, Y. W.; Wu, S.; Huang, D.; Gao, C. L.; Chen, Z. H.; McGuire, M.; Cao, T.; Xiao, D.; Liu, W. T.; Yao, W.; Xu, X. D.; Wu, S. W. Giant nonreciprocal second-harmonic generation from antiferromagnetic bilayer CrI₃. *Nature* **2019**, 572 (7770), 497-+.

(18) Song, T. C.; Cai, X. H.; Tu, M. W. Y.; Zhang, X. O.; Huang, B. V.; Wilson, N. P.; Seyler, K. L.; Zhu, L.; Taniguchi, T.; Watanabe, K.; McGuire, M. A.; Cobden, D. H.; Xiao, D.; Yao, W.; Xu, X. D. Giant tunneling magnetoresistance in spin-filter van der Waals heterostructures. *Science* **2018**, 360 (6394), 1214-+.

- (19) Xu, Y.; Ray, A.; Shao, Y. T.; Jiang, S. W.; Lee, K.; Weber, D.; Goldberger, J. E.; Watanabe, K.; Taniguchi, T.; Muller, D. A.; Mak, K. F.; Shan, J. Coexisting ferromagnetic-antiferromagnetic state in twisted bilayer CrI₃. *Nat. Nanotechnol.* **2022**, 17 (2), 143-+.
- (20) Gong, C.; Li, L.; Li, Z. L.; Ji, H. W.; Stern, A.; Xia, Y.; Cao, T.; Bao, W.; Wang, C. Z.; Wang, Y. A.; Qiu, Z. Q.; Cava, R. J.; Louie, S. G.; Xia, J.; Zhang, X. Discovery of intrinsic ferromagnetism in two-dimensional van der Waals crystals. *Nature* **2017**, 546 (7657), 265-+.
- (21) Huang, B.; Clark, G.; Navarro-Moratalla, E.; Klein, D. R.; Cheng, R.; Seyler, K. L.; Zhong, D.; Schmidgall, E.; McGuire, M. A.; Cobden, D. H.; Yao, W.; Xiao, D.; Jarillo-Herrero, P.; Xu, X. D. Layer-dependent ferromagnetism in a van der Waals crystal down to the monolayer limit. *Nature* **2017**, 546 (7657), 270-+.
- (22) Wilson, N. P.; Lee, K.; Cenker, J.; Xie, K. C.; Dismukes, A. H.; Telford, E. J.; Fonseca, J.; Sivakumar, S.; Dean, C.; Cao, T.; Roy, X.; Xu, X. D.; Zhu, X. Y. Interlayer electronic coupling on demand in a 2D magnetic semiconductor. *Nat. Mater.* **2021**, 20 (12), 1657-+.
- (23) Yang, S. Q.; Xu, X. L.; Han, B.; Gu, P. F.; Guzman, R.; Song, Y. W.; Lin, Z. C.; Gao, P.; Zhou, W.; Yang, J. B.; Chen, Z. X.; Ye, Y. Controlling the 2D Magnetism of CrBr₃ by van der Waals Stacking Engineering. *J. Am. Chem. Soc.* **2023**, 145 (51), 28184-28190.
- (24) Li, T. X.; Jiang, S. W.; Sivadas, N.; Wang, Z. F.; Xu, Y.; Weber, D.; Goldberger, J. E.; Watanabe, K.; Taniguchi, T.; Fennie, C. J.; Mak, K. F.; Shan, J. Pressure-controlled interlayer magnetism in atomically thin CrI₃. *Nat. Mater.* **2019**, 18 (12), 1303-+.
- (25) Deng, Y. J.; Yu, Y. J.; Song, Y. C.; Zhang, J. Z.; Wang, N. Z.; Sun, Z. Y.; Yi, Y. F.; Wu, Y. Z.; Wu, S. W.; Zhu, J. Y.; Wang, J.; Chen, X. H.; Zhang, Y. B. Gate-tunable room-temperature ferromagnetism in two-dimensional Fe₃GeTe₂. *Nature* **2018**, 563 (7729), 94-+.

- (26) Burch, K. S.; Mandrus, D.; Park, J. G. Magnetism in two-dimensional van der Waals materials. *Nature* **2018**, 563 (7729), 47-52.
- (27) Lu, D.; Baek, D. J.; Hong, S. S.; Kourkoutis, L. F.; Hikita, Y.; Hwang, H. Y. Synthesis of freestanding single-crystal perovskite films and heterostructures by etching of sacrificial water-soluble layers. *Nat. Mater.* **2016**, 15 (12), 1255-1260.
- (28) Zhang, J. F.; Lin, T.; Wang, A.; Wang, X. C.; He, Q. Y.; Ye, H.; Lu, J. D.; Wang, Q.; Liang, Z. G.; Jin, F.; Chen, S. R.; Fan, M. H.; Guo, E. J.; Zhang, Q. H.; Gu, L.; Luo, Z. L.; Si, L.; Wu, W. B.; Wang, L. F. Super-tetragonal $\text{Sr}_4\text{Al}_2\text{O}_7$ as a sacrificial layer for high-integrity freestanding oxide membranes. *Science* **2024**, 383 (6681), 388-394.
- (29) Chen, X. Z.; Fan, X. D.; Li, L.; Zhang, N.; Niu, Z. J.; Guo, T. F.; Xu, S. H.; Xu, H.; Wang, D. L.; Zhang, H. Y.; McLeod, A. S.; Luo, Z. L.; Lu, Q. Y.; Millis, A. J.; Basov, D. N.; Liu, M. K.; Zeng, C. G. Moire engineering of electronic phenomena in correlated oxides. *Nat. Phys.* **2020**, 16 (6), 631.
- (30) Li, Y.; Xiang, C.; Chiabrera, F. M.; Yun, S.; Zhang, H. W.; Kelly, D. J.; Dahm, R. T.; Kirchert, C. K. R.; Le Cozannet, T. E.; Trier, F.; Christensen, D. V.; Booth, T. J.; Simonsen, S. B.; Kadkhodazadeh, S.; Jespersen, T. S.; Pryds, N. Stacking and Twisting of Freestanding Complex Oxide Thin Films. *Adv. Mater.* **2022**, 34 (38), 10.
- (31) Pryds, N.; Park, D. S.; Jespersen, T. S.; Yun, S. Twisted oxide membranes: A perspective. *APL Mater.* **2024**, 12 (1), 7.
- (32) Shen, J. Y.; Dong, Z. A.; Qi, M. Q.; Zhang, Y.; Zhu, C.; Wu, Z. P.; Li, D. F. Observation of Moire Patterns in Twisted Stacks of Bilayer Perovskite Oxide Nanomembranes with Various Lattice Symmetries. *ACS Appl. Mater. Interfaces* **2022**, 14 (44), 50386-50392.

- (33) Sánchez-Santolino, G.; Rouco, V.; Puebla, S.; Aramberri, H.; Zamora, V.; Cabero, M.; Cuellar, F. A.; Munuera, C.; Mompean, F.; Garcia-Hernandez, M.; Castellanos-Gomez, A.; Iñiguez, J.; Leon, C.; Santamaria, J. A 2D ferroelectric vortex pattern in twisted BaTiO₃ freestanding layers. *Nature* **2024**, 626 (7999), 529.
- (34) Amidror, I. Moire patterns between aperiodic layers: quantitative analysis and synthesis. *J. Opt. Soc. Am. A-Opt. Image Sci. Vis.* **2003**, 20 (10), 1900-1919.
- (35) Kuwabara, M.; Clarke, D. R.; Smith, D. A. Anomalous superperiodicity in scanning tunneling microscope images of graphite. *Appl. Phys. Lett.* **1990**, 56 (24), 2396-2398.
- (36) Cao, Y.; Fatemi, V.; Demir, A.; Fang, S.; Tomarken, S. L.; Luo, J. Y.; Sanchez-Yamagishi, J. D.; Watanabe, K.; Taniguchi, T.; Kaxiras, E.; Ashoori, R. C.; Jarillo-Herrero, P. Correlated insulator behaviour at half-filling in magic-angle graphene superlattices. *Nature* **2018**, 556 (7699), 80-+.
- (37) Hunt, B.; Sanchez-Yamagishi, J. D.; Young, A. F.; Yankowitz, M.; LeRoy, B. J.; Watanabe, K.; Taniguchi, T.; Moon, P.; Koshino, M.; Jarillo-Herrero, P.; Ashoori, R. C. Massive Dirac Fermions and Hofstadter Butterfly in a van der Waals Heterostructure. *Science* **2013**, 340 (6139), 1427-1430.
- (38) Seyler, K. L.; Rivera, P.; Yu, H. Y.; Wilson, N. P.; Ray, E. L.; Mandrus, D. G.; Yan, J. Q.; Yao, W.; Xu, X. D. Signatures of moire-trapped valley excitons in MoSe₂/WSe₂ heterobilayers. *Nature* **2019**, 567 (7746), 66-+.
- (39) Chen, S. R.; Zhang, Q. H.; Rong, D. K.; Xu, Y.; Zhang, J. F.; Pei, F. F.; Bai, H.; Shang, Y. X.; Lin, S.; Jin, Q.; Hong, H. T.; Wang, C.; Yan, W. S.; Guo, H. Z.; Zhu, T.; Gu, L.; Gong, Y.; Li, Q.; Wang, L. F.; Liu, G. Q.; Jin, K. J.; Guo, E. J. Braiding Lateral Morphotropic Grain

Boundaries in Homogenetic Oxides. *Adv. Mater.* **2023**, 35 (2), 10.

(40) Chen, S. R.; Rong, D. K.; Shang, Y. X.; Cai, M. M.; Li, X. Y.; Zhang, Q. H.; Xu, S.; Xu, Y.; Gao, H. B.; Hong, H. T.; Cui, T.; Jin, Q.; Wang, J. O.; Gu, L.; Zheng, Q.; Wang, C.; Zhang, J. X.; Liu, G. Q.; Jin, K. J.; Guo, E. J. Magnetic Nanoislands in a Morphotropic Cobaltite Matrix. *Adv. Funct. Mater.* **2023**, 33 (36), 9.

(41) Fuchs D., Schwarz T.; Morán O.; Schweiss P.; Schneider R.; Finite-size shift of the Curie temperature of ferromagnetic lanthanum cobaltite thin films. *Phys. Rev. B* **2005**, 71, 092406.

(42) Torija Maria A.; Sharma M.; Gazquez J.; Varela M.; He C.; Schmitt J.; Borchers Julie A.; Laver M.; El-Khatib S.; Leighton C.; Chemically Driven Nanoscopic Magnetic Phase Separation at the SrTiO₃ (001)/La_{1-x}Sr_xCoO₃ Interface. *Adv. Mater.* **2011**, 23, 2711-2715.

(43) Wu, J.; Zheng, H.; Mitchell, J. F.; Leighton, C. Glassy transport phenomena in a phase-separated perovskite cobaltite. *Phys. Rev. B* **2006**, 73 (2), 4.

(44) Aarbogh, H. M.; Wu, J.; Wang, L.; Zheng, H.; Mitchell, J. F.; Leighton, C. Magnetic and electronic properties of La_{1-x}Sr_xCoO₃ single crystals across the percolation metal-insulator transition. *Phys. Rev. B* **2006**, 74 (13), 9.

(45) Herklotz, A.; Biegalski, M. D.; Christen, H. M.; Guo, E. J.; Nenkov, K.; Rata, A. D.; Schultz, L.; Dörr, K. Strain response of magnetic order in perovskite-type oxide films. *Philos. Trans. R. Soc. A-Math. Phys. Eng. Sci.* **2014**, 372 (2009), 12.

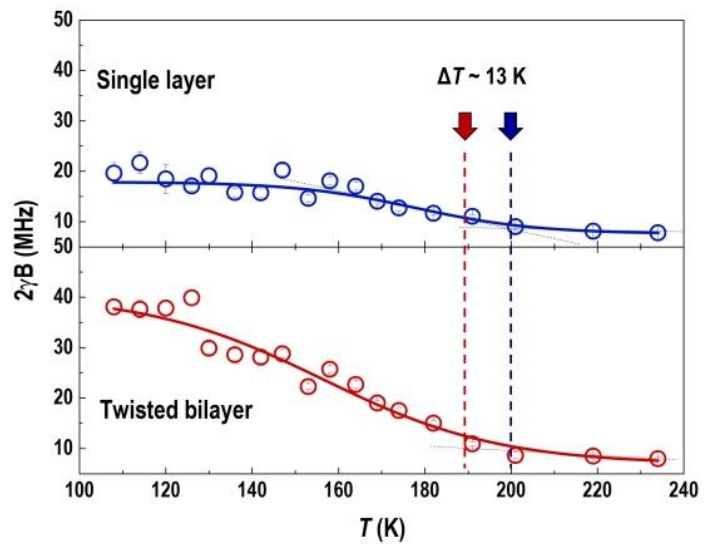
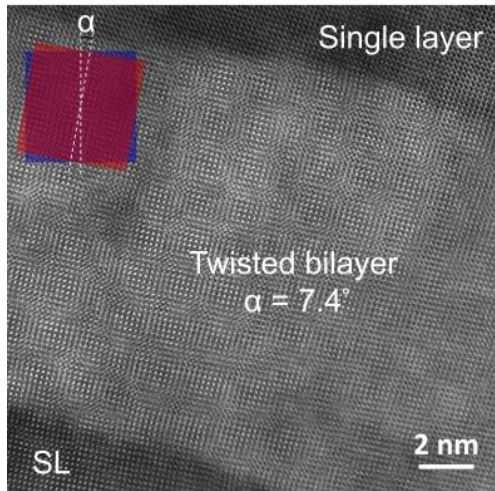
(46) Xie, H. C.; Luo, X. P.; Ye, Z. P.; Sun, Z. L.; Ye, G. H.; Sung, S. H.; Ge, H. W.; Yan, S. H.; Fu, Y.; Tian, S. J.; Lei, H. C.; Sun, K.; Hovden, R.; He, R.; Zhao, L. Y. Evidence of non-collinear spin texture in magnetic moire superlattices. *Nat. Phys.* **2023**, 19 (8), 1150.

(47) T. Kimura, S. Ishihara, H. Shintani, T. Arima, K. T. Takahashi, K. Ishizaka, and Y. Tokura,

Phys. Rev. B **2003**, 68, 060403.

(48) S. Miyasaka, Y. Okimoto, M. Iwama, and Y. Tokura, Phys. Rev. B **2003**, 68, 100406.

TOC figure



Supplementary materials for

Deteriorated Interlayer Coupling in Twisted Bilayer Cobaltites

Dongke Rong,^{†,‡} Xiuqi Chen,^{†,‡} Shengru Chen,^{†,‡,Δ} Jingfeng Zhang,[§] Yue Xu,^{†,‡}, Yanxing Shang,^{†,‡} Haitao Hong,^{†,‡} Ting Cui,^{†,‡} Qianying Wang,^{†,‡} Chen Ge,^{†,‡} Can Wang,^{†,‡} Qiang Zheng,^{||} Qinghua Zhang,^{†,‡} Lingfei Wang,[§] Yu Deng,^{⊥,*} Kuijuan Jin,^{†,‡,*} Gang-Qin Liu,^{†,‡,*} and Er-Jia Guo^{†,‡,*}

[†] Beijing National Laboratory for Condensed Matter Physics and Institute of Physics, Chinese Academy of Sciences, Beijing 100190, China

[‡] Department of Physics & Center of Materials Science and Optoelectronics Engineering, University of Chinese Academy of Sciences, Beijing 100049, China

^Δ School of Physics, Zhejiang University, Hangzhou, China

[§] Hefei National Research Center for Physical Sciences at Microscale, University of Science and Technology of China, Hefei 230026, China

^{||} CAS Key Laboratory of Standardization and Measurement for Nanotechnology, CAS Center for Excellence in Nanoscience, National Centre for Nanoscience and Technology, Beijing 100190, China

[⊥] National Laboratory of Solid-state Microstructures, Jiangsu Key Laboratory of Artificial Functional Materials, College of Engineering and Applied Sciences, Collaborative Innovation Center of Advanced Microstructures, Nanjing, Jiangsu 210023, China

[†]These authors contribute equally to the manuscript.

*Corresponding author Emails: kjjin@iphy.ac.cn, dengyu@nju.edu.cn, gqliu@iphy.ac.cn, and ejguo@iphy.ac.cn

METHODS

Sample fabrication and characterizations

The water-soluble sacrificial layer, tetragonal-phase $\text{Sr}_4\text{Al}_2\text{O}_7$ (T-SAO),²⁸ and the magnetic layer, LSCO, were epitaxially grown on (001)-oriented $(\text{LaAlO}_3)_{0.3}\text{-(Sr}_2\text{AlTaO}_6)_{0.7}$ (LSAT) substrates (*Hefei Kejing Mater. Tech. Co. Ltd*) using pulsed laser deposition (PLD). Epitaxial growth was achieved with a focused XeCl excimer laser operating at a fixed wavelength of 308 nm and an energy density of approximately 1.5 J/cm^2 . Initially, a 30 nm-thick SAO layer was deposited at a substrate temperature of 750°C and an oxygen partial pressure of 35 mTorr. Subsequently, a 5 nm-thick LSCO layer was grown at the same temperature but at a higher oxygen pressure of 200 mTorr. Upon completion of the epitaxial growth, the LSCO/SAO structure was cooled to room temperature under an oxygen pressure of 100 Torr.

Transferring freestanding membranes to STEM grids

A thermal-release tape (TRT) was affixed to the LSCO films, forming a TRT/LSCO/SAO/LSAT structure. The sample was then submerged in deionized (DI) water at room temperature. Upon the complete dissolution of the sacrificial SAO layer, the LSCO layer detached from the substrates. Subsequently, the TRT/LSCO assembly was transferred onto a NaCl crystal. By heating up the sample to 110°C for 3 minutes, the TRT lost its adhesion, allowing for easy removal while the LSCO layer remained securely attached to the NaCl crystal. During the transfer of the second LSCO layer, a transfer platform was used to precisely control the rotational angle of the first LSCO layer. After releasing the twisted bilayer (BL) LSCO onto the NaCl crystal, PMMA (950, A5) was spin-coated onto the surface of the bilayer LSCO sample at 2000 rpm and heated at 110°C for 10 minutes to serve as a new supporting layer.

The PMMA/BL LSCO/NaCl assembly was then immersed in DI water. Upon the dissolution of NaCl, the PMMA/BL-LSCO bilayer floated on the water's surface. Subsequently, the PMMA/BL-LSCO was transferred onto a copper grid. Finally, the PMMA support was removed using acetone, leaving a clean twisted BL LSCO.

STEM measurements

These STEM measurements were performed at various microscopy laboratories, including the Institute of Physics (IOP), the National Centre for Nanoscience and Technology (NCNT) of the Chinese Academy of Sciences (CAS), and the Collaborative Innovation Center of Advanced Microstructures at Nanjing University. The samples were directly transferred onto copper grids and imaged along the (001) zone axis of LSCO. STEM imaging was conducted using a double-Cs-corrected Titan Cubed G2 60-300 kV microscope (Thermo Fisher Scientific). The microscope was operated at an accelerating voltage of 300 kV, with a convergence angle of 25 mrad and an annular dark field (ADF) collection angle ranging from 60 to 200 mrad. All aberrations up to the third order were corrected to achieve a phase shift of less than $\pi/4$ at 20 mrad. The electron probe was optimized to a size of approximately 0.8 Å. Images were acquired with dwell times ranging from 1.0 to 2.0 seconds and a frame size of 1024×1024 pixels. Atomic distances between A-site atoms were determined by fitting intensity peaks with Gaussian functions. The STEM data analysis and fast Fourier transform (FFT) processing were performed using Gatan Digital Micrograph software.

NV magnetometry

Spatially resolved magnetic measurements were performed using a home-built optically detected magnetic resonance (ODMR) system. The ODMR spectra were obtained by sweeping

the microwave frequency and recording the PL signals of the focused NV centers. At an ideal zero field, the $m_S = \pm 1$ states of an NV center are degenerated and there is only one dip in the ODMR spectrum. However, if the sample has a stray field from LSCO membranes, the transition frequencies of $m_S = +1$ ($m_S = -1$) to $m_S = 0$ are linearly shifted due to the Zeeman effect, resulting in a splitting of the ODMR spectra. The strength of the stray field emanating from the sample was estimated by fitting the ODMR spectra with a two-peak Lorentz function. It is worth noting that more than a thousand NV centers were measured in a single laser spot, and the gradient of the stray field causes additional broadening of the ODMR spectra (Fig. S10). Meanwhile, there is an intrinsic ODMR splitting (about 8.2 MHz) for the measured NV centers, which can be attributed to the randomly distributed charges in the diamond lattice. The sample temperature was controlled with the cryostat (Montana Instruments, S100) and monitored with a thermometer glued to the sample stage. The temperature stability of the system was estimated to be better than 0.5 K.

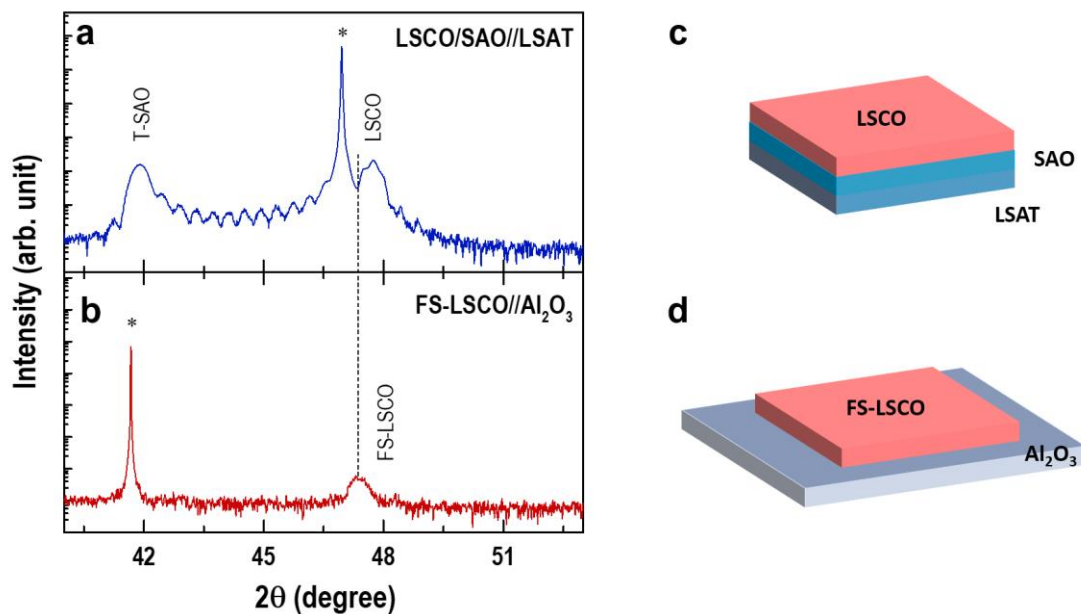


Figure S1. Structural characterizations of epitaxial growth LSCO films and freestanding (FS) LSCO membranes. (a) XRD 2θ - ω scans of the LSCO/SAO bilayer grown on (001)-oriented LSAT substrates. Both LSCO and tetragonal phase SAO (T-SAO) films show distinct Laue oscillations, indicating high-quality epitaxial growth. (b) XRD 2θ - ω scan of a FS-LSCO transferred onto a (0001)-oriented Al_2O_3 substrate. (c) and (d) Schematics of epitaxial grown LSCO/T-SAO bilayer and FS-LSCO membranes. The slightly shift of FS-LSCO's diffraction peak compared to that of the LSCO epitaxial film suggests a relaxation of tensile strain in LSCO.

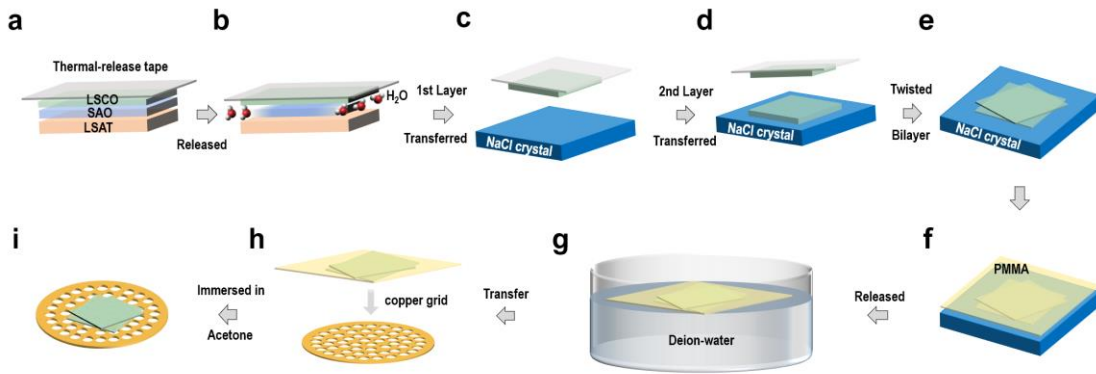


Figure S2. Transfer process of twist BL LSCO. (a) Attach TRT to the LSCO surface. (b) Dissolve SAO layer into DI water. (c) Transfer the 1st FS-LSCO membrane and (d) transfer the 2nd FS LSCO layer onto a NaCl crystal. (e) Twist BL LSCO with a twist angle on a NaCl crystal. (f) Spin-coat the PMMA on the twisted BL LSCO. (g) Placed the sample in the DI water. After the NaCl substrate dissolved, the PMMA/BL LSCO is floating on the water's surface. (h) Attach the PMMA/BL LSCO to the copper grid. (i) Removal of PMMA film by acetone. More detailed transfer methods can be found in the experimental section.

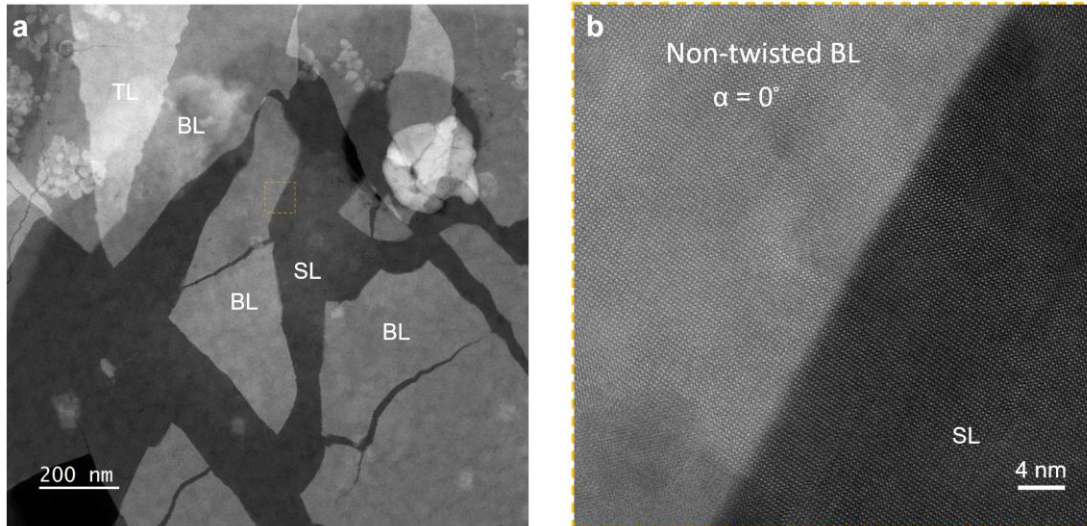


Figure S3. STEM images of the twist BL LSCO. (a) Low-magnified STEM image of the twist BL LSCO. Single-layer (SL), bilayer (BL) and trilayer (TL) regions can be observed from this image. However, it is evident from this image that the FS LSCO exhibits partial damage, resulting from the wet transfer process. (b) High-magnified STEM image of a represent region containing both SL and BL. Notably, no twist angle was observed in the BL region, hence no moiré patterns emerge in this area.

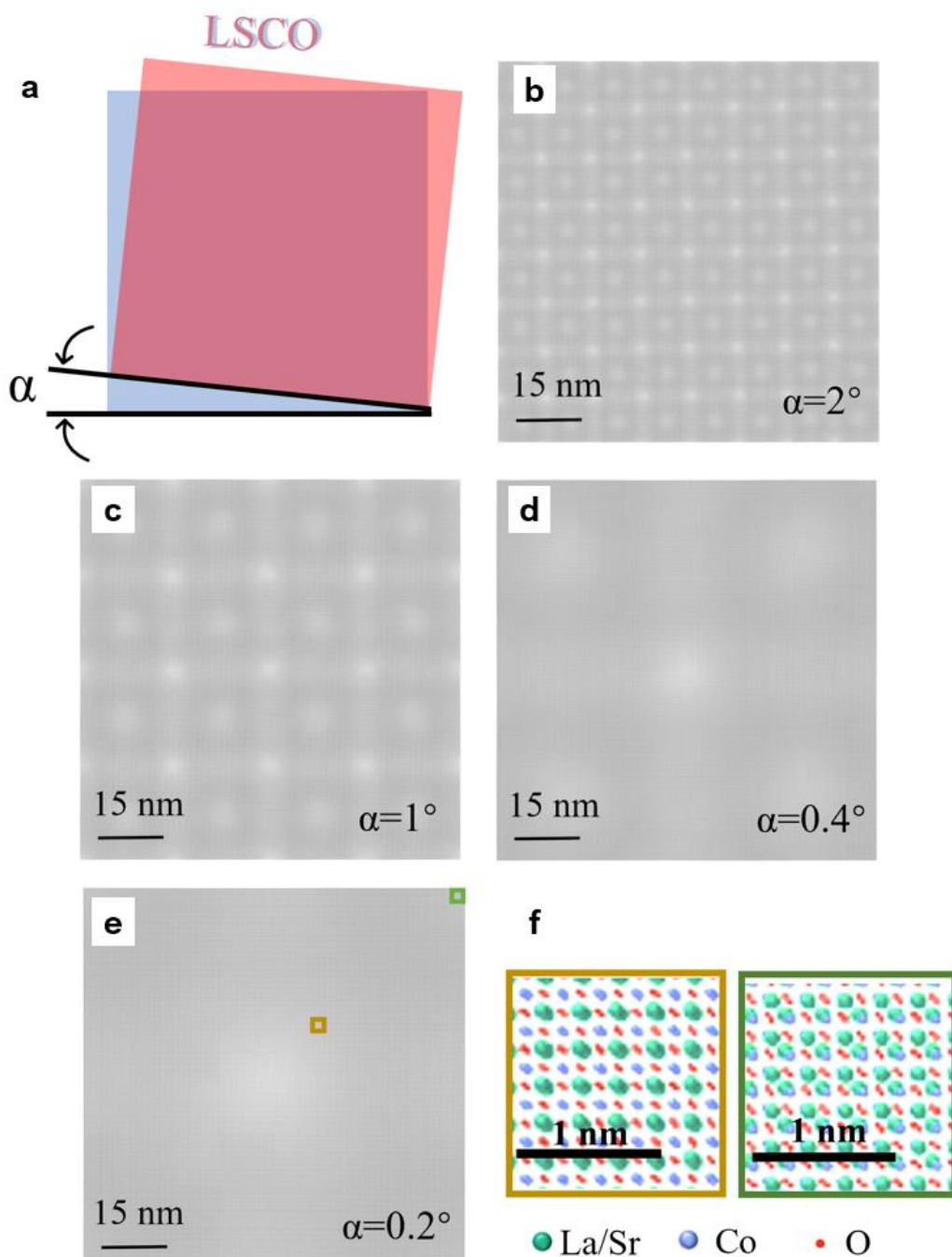


Figure S4. Simulations of moiré patterns and atomic images of twisted BL LSCO. (a) Schematic representation of the α structure. (b-e) Simulated patterns for the α structure with twist angles ranging from 2° to 0.2° . Across all α values, the pattern shape remains consistent, with smaller α values corresponding to larger periods. This suggests that the Moiré pattern can effectively indicate small twist angles, down to 0.2° . (f) Simulated atomic images within the brown and green frames in (e). These images are sensitive to both the twist angle and position, suggesting that atomic resolution observations can be employed to identify very small twist angles.

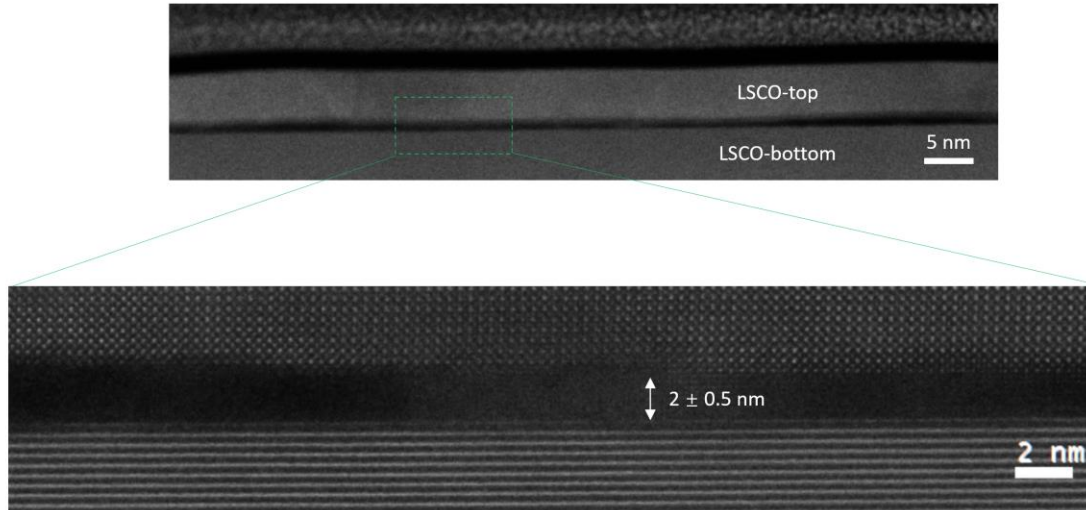


Figure S5. Cross-section STEM image at the interface between twisted BL LSCO. The bottom shows the zoom-in STEM image at a representative interface, illustrating a gap with approximately 2 ± 0.5 nm.

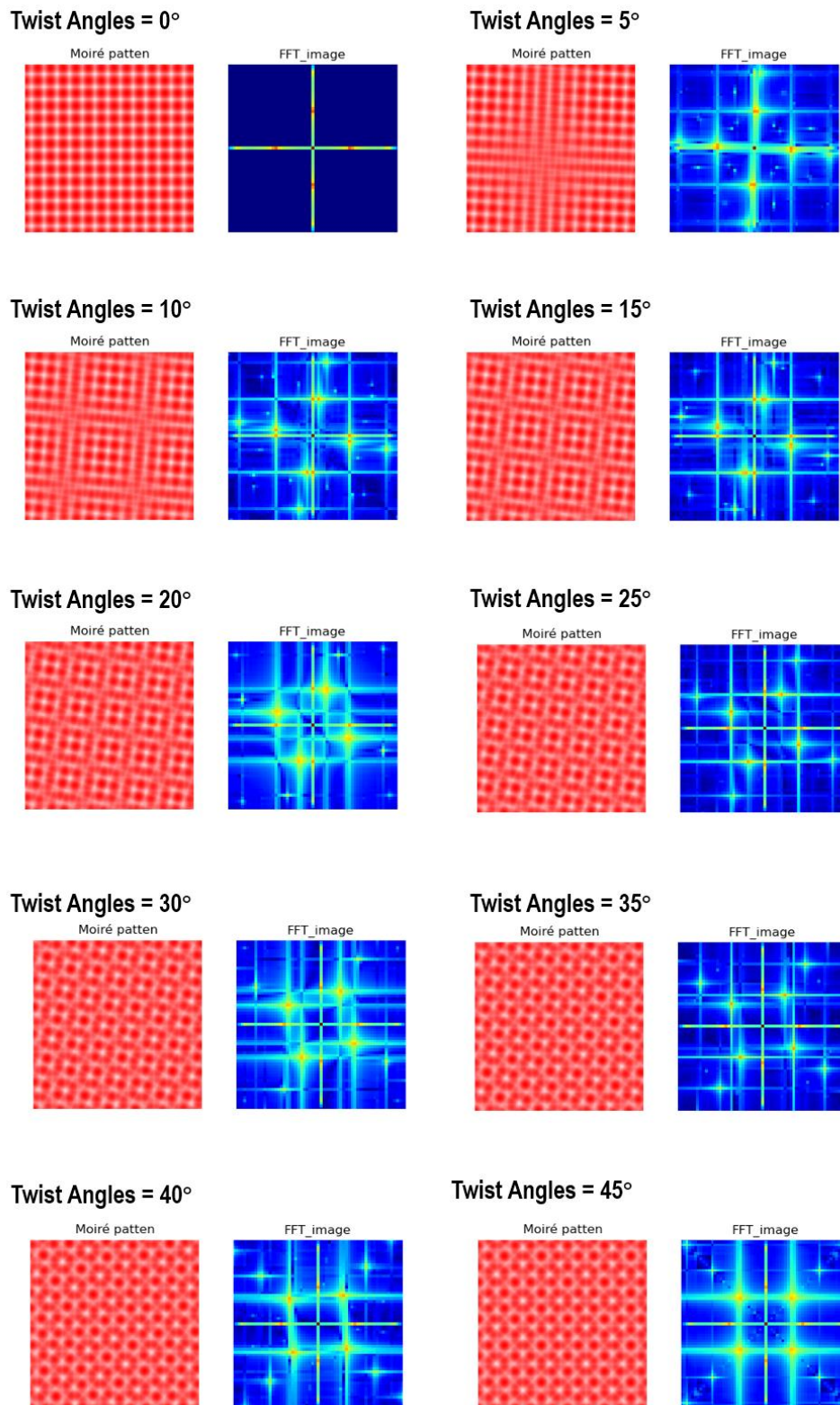


Figure S6. Simulated moiré patterns and FFT results in BL LSCO with different twist angles.

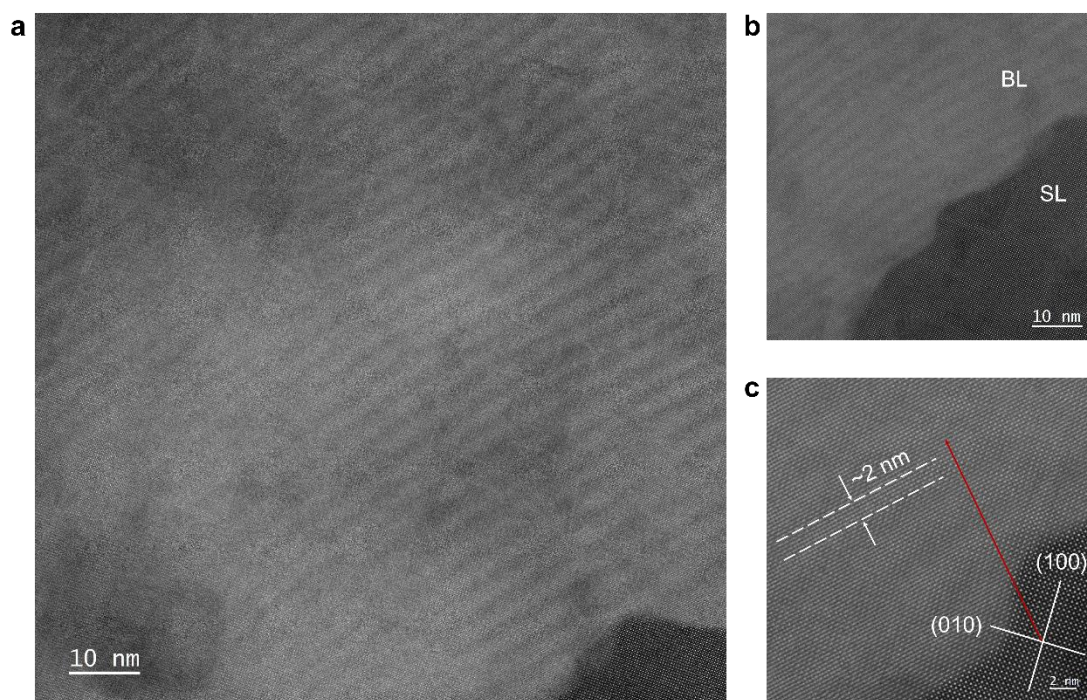


Figure S7. Stripe-like moiré patterns in the twist BL LSCO. (a) Low-magnified STEM image of the stripe-like moiré patterns. (b) A representative high-resolution STEM image. (c) The high-resolution image reveals the strips have an angle of 45 degrees with respect to both (100) and (010) orientations of FS LSCO. The width of stripe patterns is approximately 2 nm. The stripes are exclusively observed in the BL region, indicating a distinct moiré effect different from the classical moiré patterns shown in the main text.

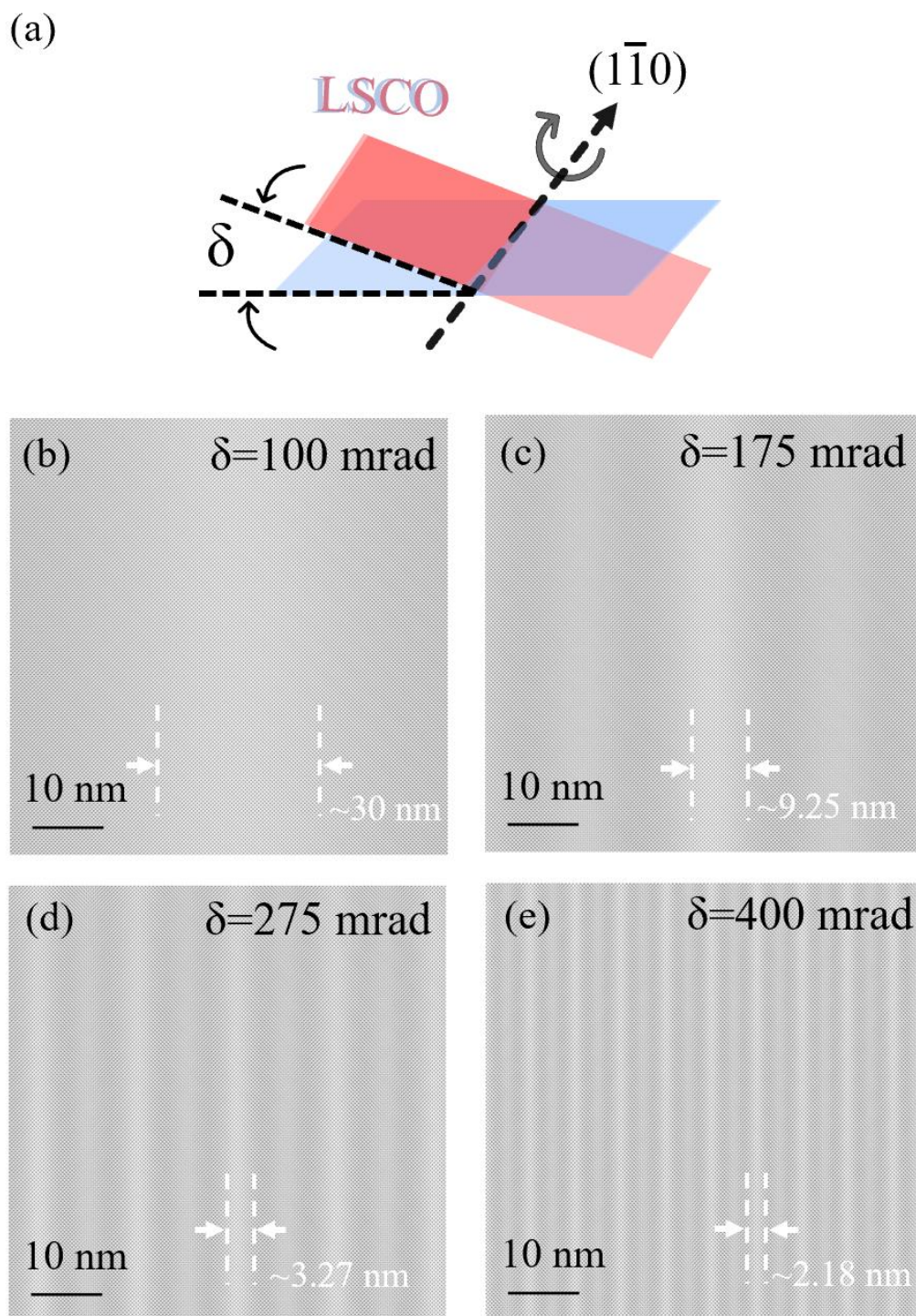


Figure S8. Simulated tilt structure patterns of BL LSCO with different tilts (δ). (a) Diagram of the BL LSCO structure with a titled zone axis. (b-e) Simulated patterns.

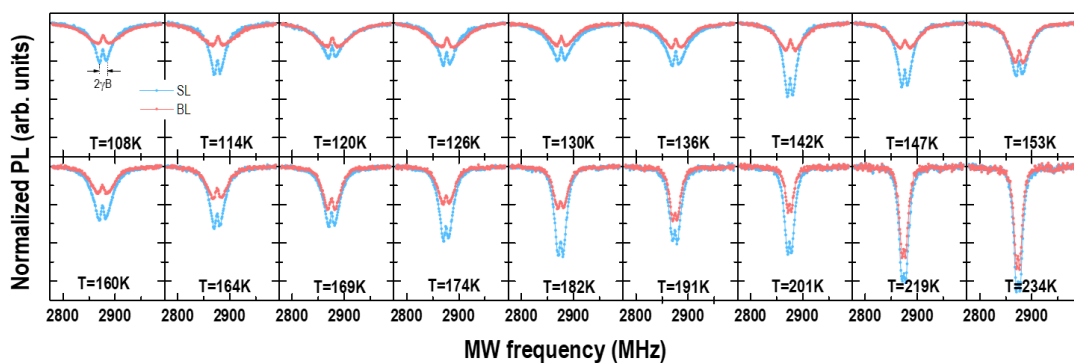


Figure S9. ODMR spectra at SL and BL regions in the twist BL LSCO. As the temperature increases, the peak splitting reduces. The temperature dependent peak splitting at the SL and BL regions are plotted in Figure 3d of the main text.

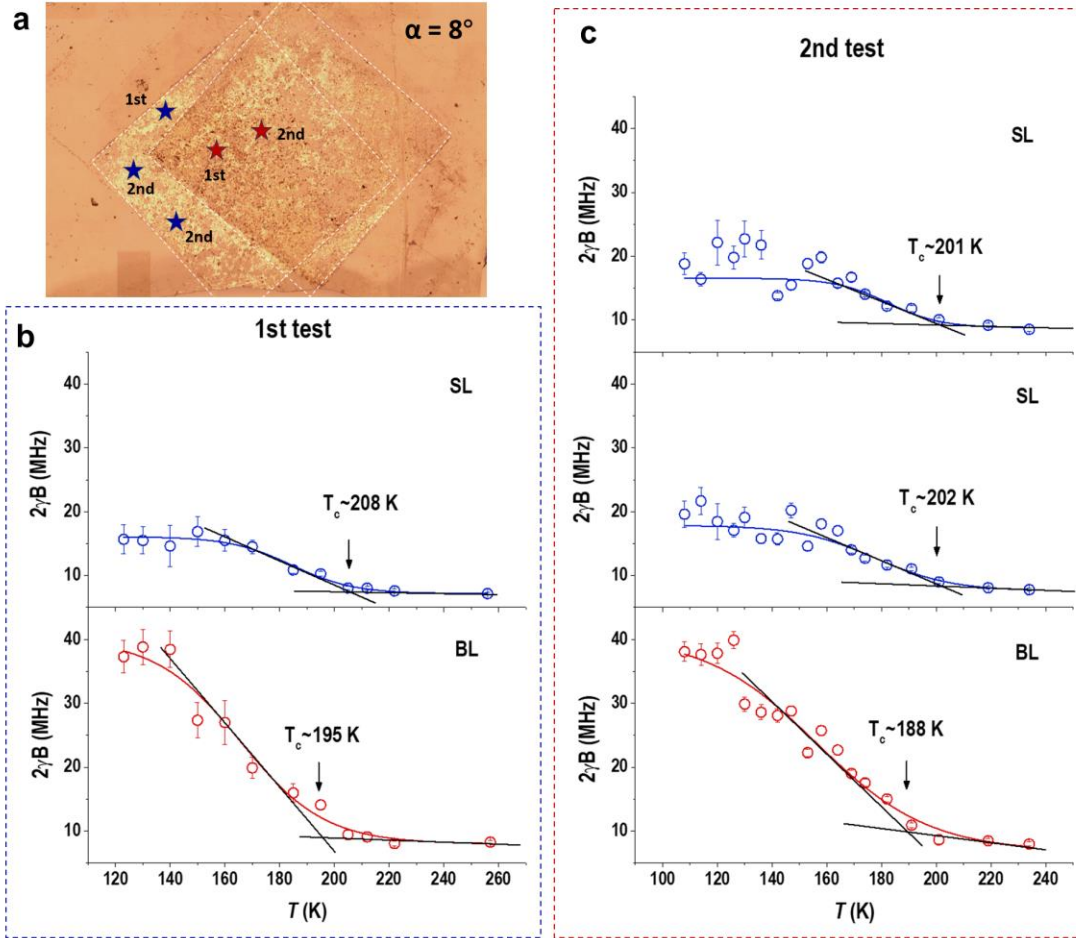


Figure S10. Consistent measurements at different locations in SL and BL LSCO. (a) Optical image of the twisted BL LSCO, with colored stars indicating the locations where NV magnetometry was performed. (b) and (c) Results of the first and second NV ODMR measurements. These results show that the critical temperature (T_C) of SL LSCO is approximately 204 ± 5 K, while the T_C of BL LSCO is approximately 191.5 ± 3.5 K. The T_C of BL LSCO is therefore consistently lower than that of SL LSCO.

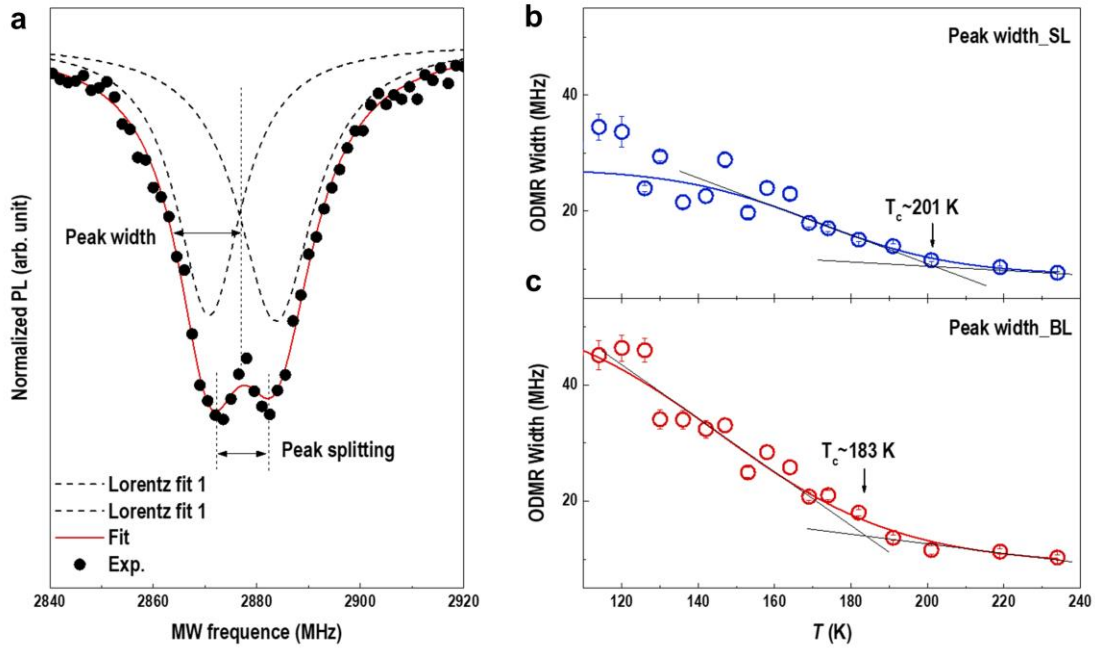


Figure S11. Temperature-dependent ODMR width in SL and BL regions. (a) A representative ODMR spectrum, in which the width and splitting of the resonant dips are defined. Dashed lines are the Lorentz fits to the experimental data. The red line is the sum-up results of two Lorentz fits. (b) and (c) Temperature-dependent ODMR width in SL and BL LSCO regions, respectively.

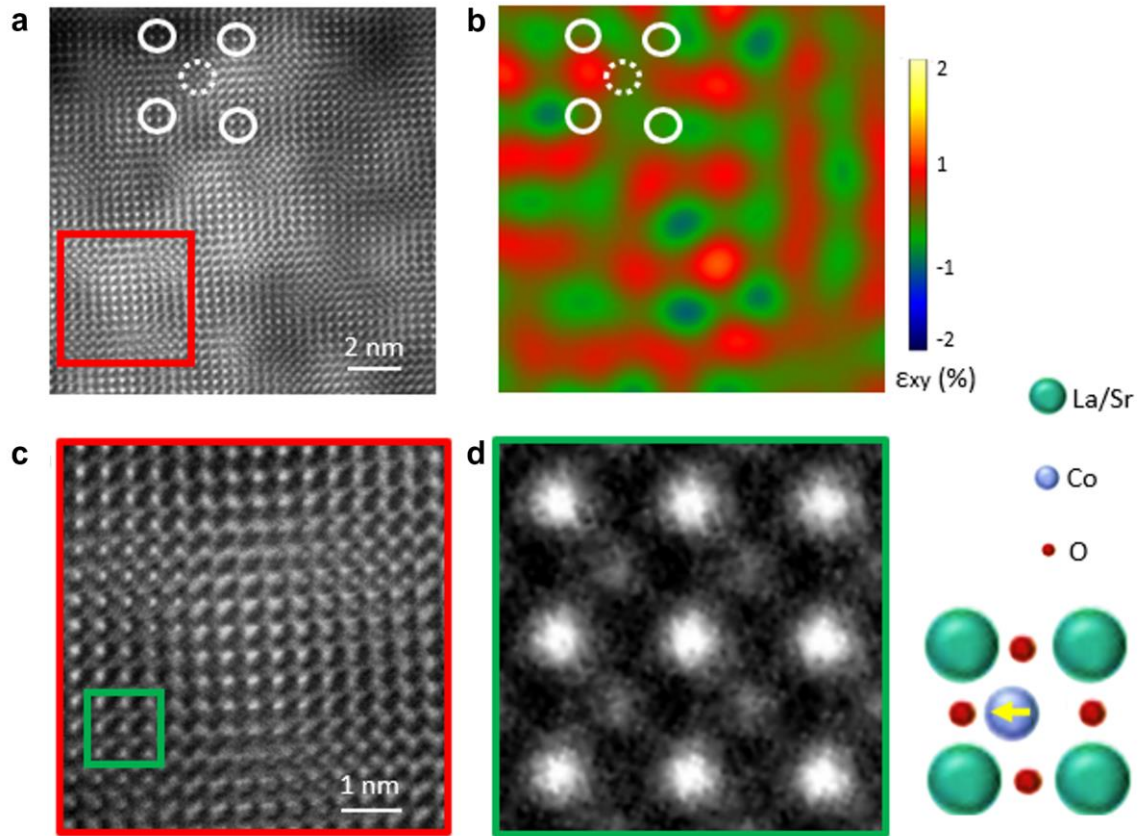


Figure S12. Strain modulations of a twisted BL LSCO, and the Co off-site in the strained LSCO lattice. (a) STEM-HAADF image of a twisted LSCO, with its Fast Fourier transform (FFT) (in the main text Figure 2b) in the below inset, showing a 8° twist angle. (b) The shear strain mapping of (a) (ϵ_{xy} is component of the lattice strain tensor) depicts a periodic strain modulation at the top LSCO layer. (c) and (d) Zoom-in HRSTEM observations of the Co off-site in the strained LSCO.